applied sciences

MDPI

Article

Investigation of Size Effects Due to Different Cooling Rates of As-Quenched Martensite Microstructures in a Low-Alloy Steel

Marius Graf [1,2,*], Matthias Kuntz [1,*], Hermann Autenrieth [1] and Ralf Müller [2]

[1] Robert Bosch GmbH, Corporate Research, 71272 Renningen, Germany; hermann.autenrieth@de.bosch.com
[2] Institute of Applied Mechanics, TU Kaiserslautern, 67653 Kaiserslautern, Germany; ram@rhrk.uni-kl.de
* Correspondence: marius.graf@de.bosch.com (M.G.); matthias.kuntz2@de.bosch.com (M.K.); Tel.: +49-711-811-56430 (M.G.); +49-711-811-34413 (M.K.)

Received: 2 June 2020; Accepted: 1 August 2020; Published: 4 August 2020

Featured Application: The results of this work will be used to develop simulation models that will be applied in the early development stages of highly stressed components. A further aim is that these investigations might contribute to a better understanding of the martensite transformation mechanism.

Abstract: Martensite transformation is a complex mechanism in materials that is classically initiated by a suitable heat treatment. This heat treatment process can be optimized based on a better understanding of the physical mechanisms on the length scale of several prior austenite grains. It is therefore appropriate to consider individual process steps of heat treatment in isolation. The aim of this study is to characterize the microstructural size changes caused by a variation of the cooling rate applied during the quenching process. For this purpose, individual martensitic microstructures from different heat treatments are analyzed using the electron backscatter diffraction (EBSD) method. With special orientation relationships between the parent austenite and martensite, the structure of the prior austenite grains and the close packet plane packets can then be reconstructed. The influence of the heat treatments on these characteristics as well as on the martensite blocks is thus quantified. No significant influence of the quenching rate on the sizes of martensite blocks and packets could be found.

Keywords: EBSD; 50CrMo4; SAE 4150; quenched and tempered steel; martensite transformation; nucleation

1. Introduction

The microstructure of materials has a significant influence on the macroscopic material and component behavior [1,2]. Regarding steels, martensite is an often-desired microstructure due to its hardness. Usually, martensite is produced with an appropriate heat treatment. Martensite of the α' type has been observed to be the most common in ferrous martensite. In [3], five morphology types of α' martensite are reported: lath, butterfly, $(225)_\gamma$ plate type, lenticular and thin plate. These different morphologies arise depending of the chemical composition and the start temperature of martensite T_{MS}. The listed martensite types occur with decreasing T_{MS} in the order mentioned above. Besides T_{MS}, the strength of the parent austenite and product martensite and the critical resolved shear stress for slip and twinning, as well as the cooling rate, seem to be determining factors for the resulting morphology [4–8]. Otherwise, the factors are rather poorly defined [9]. This work focuses on the lath morphology.

The crystallography of lath martensite has been examined in [10,11] using Kikuchi patterns and electron backscatter diffraction (EBSD) analysis. In these works, Fe-C alloys with different carbon contents are analyzed. Typical structures consist of a three-level hierarchy [12]: martensite laths, blocks and packets. Within this hierarchy, several laths form a block, whereby the laths are martensite crystals with the same orientation (with 0–0.4% C) or two different orientations (with $\approx$ 0.6% C) depending on the carbon content [11]. Several blocks with the same close packet plane (CPP) form a packet. Since a prior austenite grain (PAG) has four CPPs, several packets can be formed in it.

The packet and block sizes can significantly affect the mechanical properties of the considered materials [13,14], which can be explained by grain boundary strengthening according to the Hall–Petch strengthening mechanism [15,16]. As a consequence, there is an interest in quantifying such size effects in order to predict the structure–property relationships.

The resulting martensite sizes are determined by various factors. It has been observed that packet and block sizes decrease with increasing carbon content [11]. In [17], a correlation between PAGs and the packet size as well as the block thickness was found. With a finer austenite grain structure, a finer packet and block structure is achieved. The lath size is almost insensitive to changes in the prior austenite grain sizes [14,18]. Furthermore, higher cooling rates can lead to finer packet and block structures [19–24]. However, no size effect with regard to the cooling rate was found in [25]. The effects of process parameters related to induction hardening on phase transformation including microstructure size effects were recently investigated in [26–34].

With a focus on the influence of cooling rates on martensite transformation, constant martensite start temperatures (or at least martensite start temperatures that are not systematically dependent on the cooling rate) indicate an athermal initial nucleation mechanism. Based on the review given in [8], the research group of Shastlivtsev [7,35–37] conducted extensive investigations on the influence of cooling rates on the structure and phase state of iron and low-alloy carbon steels. Accordingly, a fast isothermal martensitic transformation takes place in steels with low and medium carbon contents at moderate cooling rates. At high cooling rates, an athermal mechanism of martensitic transformation was observed. Regarding steels with carbon concentrations $\geq$ 0.7 wt%, an athermal mechanism of martensitic transformation was already observed at moderate cooling rates. The absence of an influence of the cooling rate on the kinetics of martensite formation was confirmed for plain carbon Fe-0.8 wt% [38] and FeNiCoMo alloy [39].

With regard to resulting size effects on the microstructure, several discussions can be found in the literature. In [23], a modulated martensite formation in a Fe-22 wt% Ni alloy was investigated. It was concluded that subsequent simultaneous block formation is influenced by thermally activated local stress relaxation. Based on [22], it can be argued that the quenching rate influences the volume fraction gradient concerning temperature. With shorter cooling times, more martensite is formed at lower temperatures, which means a higher resistance against lattice displacement, resulting in higher stresses. From an energetic point of view, it is therefore beneficial to minimize the stresses by formation of a finer block structure. Another explanation was formulated in [27]. Thus, due to the higher cooling rate, the amount of dislocation increases. These lattice defects may act as nucleation sites for martensite. Additional higher driving forces lead to an increase in the growth rate of martensite.

In this work, the microstructure of different quenched specimens is evaluated by means of EBSD. Based on the orientations, the cross-sections of martensite blocks are reconstructed and analyzed. In addition to [22], the CPPs and PAGs are reconstructed based on the martensite orientation relationship. With this method, sections of the microstructure on the scale of representative volume elements can be evaluated, resulting in a statistically significant amount of data. The findings of this work serve as an essential basis for the development of novel simulation models that describe the evolution of martensite on microstructure length scales in order to contribute to our understanding of martensite transformation.

2. Experimental Setup and Methodology

For the experimental investigations in this work, referring to previous studies, the material 50CrMo4 (SAE 4150) is used [1,22,40,41]. For the sake of completeness, mean values of the chemical composition are documented in Table 1. These values were determined by spark emission spectroscopy analysis [1]. The initial material condition is pre-hardened.

Table 1. Chemical composition of the investigated material 50CrMo4 (SAE 4150) in wt.%; the remainder is Fe.

Material	C	Si	Mn	P	S	Cr	Mo
50CrMo4 [1]	0.52	0.26	0.74	0.014	0.008	1.31	0.18

Different types of cylindrical specimens are heat-treated in order to form a homogeneous and purely martensitic microstructure. In Figure 1a, the three types are depicted with their nominal dimensions. Types A and B are analyzed with regard to the morphology of their martensite structure. The reason for the hole in type B is that, due to the reduced mass, a higher quenching rate is achieved with the same quenching medium. Specimen type C only serves as an accompanying specimen to measure the temperature inside. The temperature is measured with a thermocouple (type K), which is inserted and fixed in the blind hole of specimen type C.

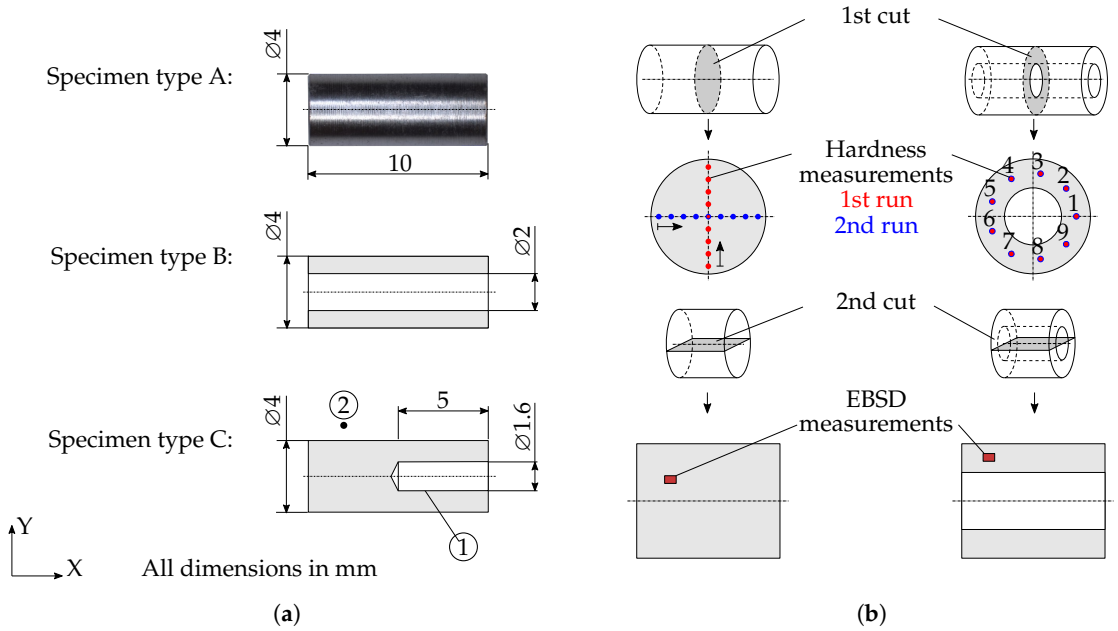

Figure 1. Specimen geometry and measurement methodology, (**a**) Specimen types with nominal dimensions of material 50CrMo4 (SAE 4150); specimen type C is only used for temperature measurement. (**b**) Specimen handling after heat treatment. EBSD: electron backscatter diffraction.

In order to achieve different quenching rates, two different heat treatment processes were used. The first was performed with the dilatometer DIL 805A from TA Instruments. Specimens of type A and B were heated by induction at a rate of 20.0 Ks^{-1} to a temperature of 860 °C. A vacuum in the chamber containing the specimen prevented the decarburization of the surface layer of the specimen. For supercooling, the chamber was flooded with nitrogen, where a linear temperature curve was specified. The temperature was measured with a type S thermocouple. With this experimental setup, the critical quenching rate necessary to obtain a fully martensitic microstructure was determined step by step with specimen type A. Furthermore, the highest cooling rate possible with this test configuration was tested with specimen types A and B.

As the quenching rate of the dilatometer was limited, a second experimental setup was used. With this setup, specimen types A and C were heated in a furnace and then quenched in a water bath. The temperature inside (①) and outside (②) the specimen was measured; see Figure 1a. With both experimental setups, a holding time of 30 min at high temperature was employed to guarantee full austenitization.

After heat treatment, the specimens were divided crosswise as depicted in Figure 1b. In order to check the homogeneity of the microstructure, hardness measurements were taken on the new surface highlighted in gray with the low-load Vickers hardness tester KB30 BVZ. Two runs of measurements were performed in each case. Before each run, the specimens were ground and polished (final polishing step: 3.0 µm diamond suspension).

A second cut lengthwise exposed the surface on which the microstructure was characterized; see Figure 1b. For the EBSD analyses, the surface was ground with SiC sand paper with grades up to 4000 followed by diamond polishing with suspension sizes of 3.0 µm and 1.0 µm. The final polish was performed with a 0.06 µm aluminum suspension (Eposal). The EBSD measurements were performed with the scanning electron microscope Zeiss Supra 55 VP. Areas of 114 µm × 85 µm with a step size of 0.15 µm were measured. Only phases that could be assigned to martensite or retained austenite were indexed. After the analysis was performed at a suitable location, the surface was etched with 1% alcoholic HNO3 (Nital) in order to analyze the location with optical microscopes (Axioimager.M2m and Axioplan 2 Imaging) to check whether a completely martensitic structure was present.

In order to calculate the high-temperature austenite grains, the python tool ARPGE (version 2.4) [42] was used. The visualization, as well as the evaluation of the morphology, was performed with the Matlab toolbox MTEX 5.1.1. [43].

3. Experimental Results

To differentiate different heat treatments, cooling times from 800 °C to 500 °C (t_{85}), from 800 °C to 100 °C (t_{81}) and from the martensite start temperature T_{MS} to 100 °C ($t_{T_{\mathrm{MS}}\rightarrow 100\,^{\circ}\mathrm{C}}$) were used. Furthermore, the approximated quenching rates

$$\dot{\bar{T}}_{85} = \frac{800\,^{\circ}\mathrm{C} - 500\,^{\circ}\mathrm{C}}{t_{85}}, \quad \dot{\bar{T}}_{\mathrm{T_{MS}}\rightarrow 100\,^{\circ}\mathrm{C}} = \frac{T_{\mathrm{MS}} - 100\,^{\circ}\mathrm{C}}{t_{T_{\mathrm{MS}}\rightarrow 100\,^{\circ}\mathrm{C}}} \quad \text{and} \quad \dot{\bar{T}}_{81} = \frac{800\,^{\circ}\mathrm{C} - 100\,^{\circ}\mathrm{C}}{t_{81}} \tag{1}$$

were defined.

3.1. Heat Treatment

In Figure 2a, the dilatation curves of the specimens during the heating are shown. The linear course of all curves from a temperature of 825 °C indicates that, for all specimens, full austenitization is achieved. Figure 2b shows the corresponding dilatation curves during the quenching. Concerning the martensite start temperature, no significant influence of the quenching rate is observed. However, the yellow curve corresponding to $t_{85} = 30.5$ s has a different gradient, which indicates the formation of a non-martensitic phase at high temperature. All other curves show a parallel course. Thus, the critical time interval is $t_{85} = 20.0$ s, corresponding to a quenching rate of $\dot{\bar{T}}_{85} = 15.0\,^{\circ}\mathrm{Cs}^{-1}$.

The temperature curves with respect to time in Figure 2c are extended by the temperature measurements during the water bath quenching. The reduction of the temperature rate at approximately the martensite start temperature is due to the exothermic austenite–martensite transformation. The black dashed lines indicate the corresponding ideal linear course. Based on this diagram, the parameters t_{85} and $\dot{\bar{T}}$ can be determined. Accordingly, by using water as quenching medium, a time interval of $t_{85} = 0.62$ s corresponding to a quenching rate of $\dot{\bar{T}}_{85} = 484\,^{\circ}\mathrm{Cs}^{-1}$ is achieved inside the sample.

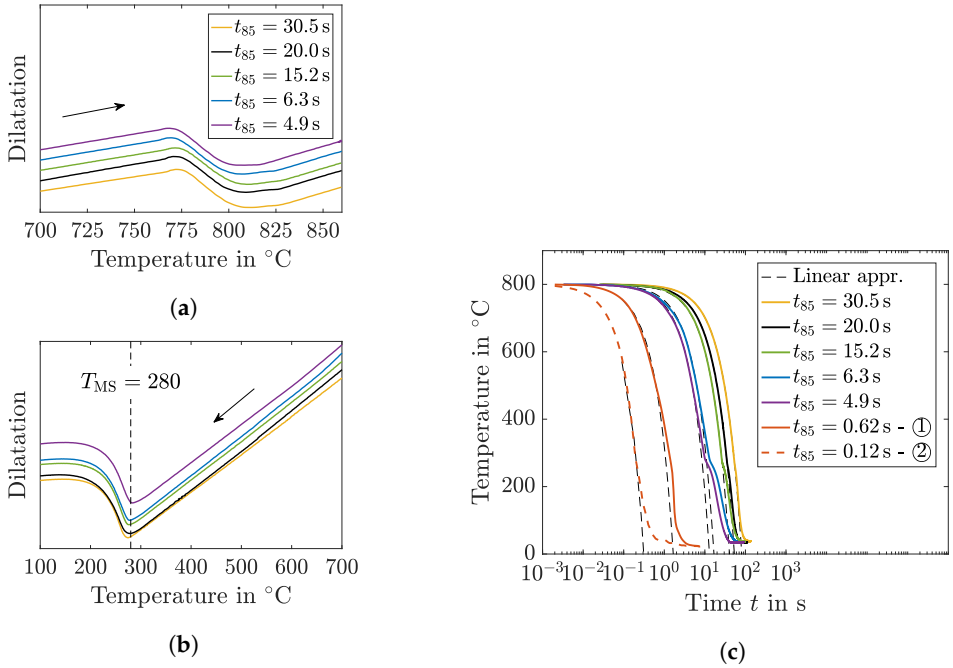

Figure 2. Heat treatment of the specimens, (**a**) dilatation curves of SAE 4150 during heating, (**b**) dilatation curves of SAE 4150 during cooling, (**c**) temperature profile during cooling. Note that temperature curves are time-shifted so that $T(t = 0) = 800\,^{\circ}\mathrm{C}$.

Four heat treatments were selected for the next analysis step, which are summarized in Table 2 with their respective cooling times. The further investigated test runs corresponded to the lowest possible quenching rate to form a fully martensitic microstructure, the maximal possible quenching rate with specimen types A and B with the dilatometer setup and the water bath quenching rate, which is the overall maximum rate investigated in this work. Note that the dilatometer with the chosen quenching medium could not keep the specified cooling rate below the martensite start temperature. As a result, the sample from analysis A2 experienced slower cooling below T_{MS}.

Table 2. Relevant measured quenching parameters and martensite start temperatures of EBSD-analyzed specimens; parameters for A4 refer to measuring point ①.

Analysis **Specimen Type**	**A1** **A**	**A2** **A**	**A3** **B**	**A4** **A**
T_{MS} in °C	279.3	277.1	286.8	-
t_{85} in s	20.0	6.3	4.9	0.62
$t_{T_{MS}\to 100\,^{\circ}\mathrm{C}}$ in s	18.1	20.1	15.3	0.47 *
t_{81} in s	52.8	33.5	25.0	1.9
$\dot{\bar{T}}_{85}$ in $^{\circ}\mathrm{Cs}^{-1}$	15.0	47.6	61.2	484
$\dot{\bar{T}}_{T_{MS}\to 100\,^{\circ}\mathrm{C}}$ in Ks^{-1}	9.9	8.8	12.2	383 *
$\dot{\bar{T}}_{81}$ in $^{\circ}\mathrm{Cs}^{-1}$	13.3	20.9	28.0	368

* underlying assumption: $T_{MS} = 280\,^{\circ}\mathrm{C}$.

3.2. Hardness

The results of the hardness measurements for each test run and specimen are depicted in Figure 3. In these diagrams, the deviation from the overall mean per specimen is given depending on the position number. Here, we show that, with the chosen specimen geometry and the heat treatment with the first experimental setup, a homogeneous hardness course, and thus a homogeneous martensite

structure, is obtained. Regarding the fourth specimen (Figure 3d), decarburization took place at the edge of the specimen. Outside the surface layer zone, however, a homogeneous structure is achieved.

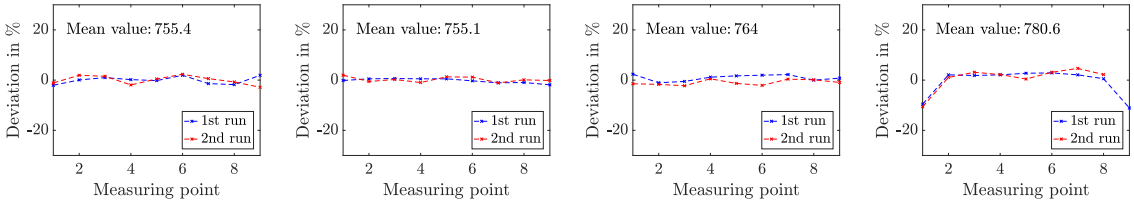

Figure 3. Variation of the hardness measurements by indicating the deviation from the mean value of the individual samples (**a**) A1, (**b**) A2, (**c**) A3, (**d**) A4.

In Figure 4, the correlation between the quenching rate and the hardness is shown. By increasing the cooling rate, a higher hardness is obtained.

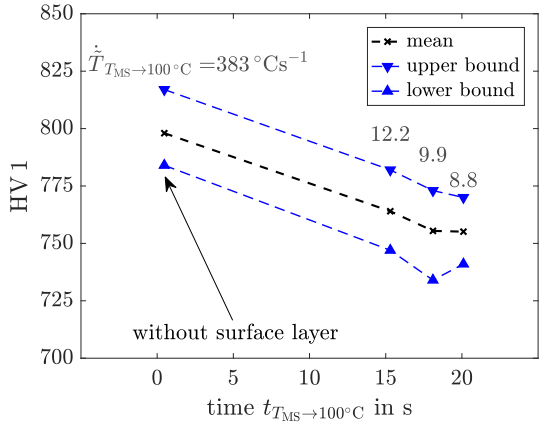

Figure 4. Correlation between measured hardness and cooling time; numbers above data points indicate cooling rates.

3.3. Microstructure Analyses

The results of the EBSD analyses are shown as orientation maps in Figure 5, where the inverse pole figure (IPF) color scheme is used for the illustration of the martensite orientations. Note that the raw data have been smoothed and filtered using the half-quadratic minimization of manifold-valued data [44]. Within the measuring accuracy, no retained austenite could be detected for all heat treatments. In accordance with [30], the present measured orientations confirm the Kurdjumov–Sachs [45] orientation relationship. Based on this, PAG boundaries are automatically reconstructed and depicted as black lines in Figure 5. White lines indicate recrystallization twin boundaries of PAGs, which are identified via their special orientation to each other. Contrary to expectations, in several cases, the (twin) boundaries follow somewhat jagged lines, which is a sign that some orientations have been misindexed. This can be attributed to the fact that austenite grains and their twins share equal martensite variants. A detailed discussion about this can be found, for example, in [46]. In the context of the statistical analyses in the present study, twins are considered as single PAGs.

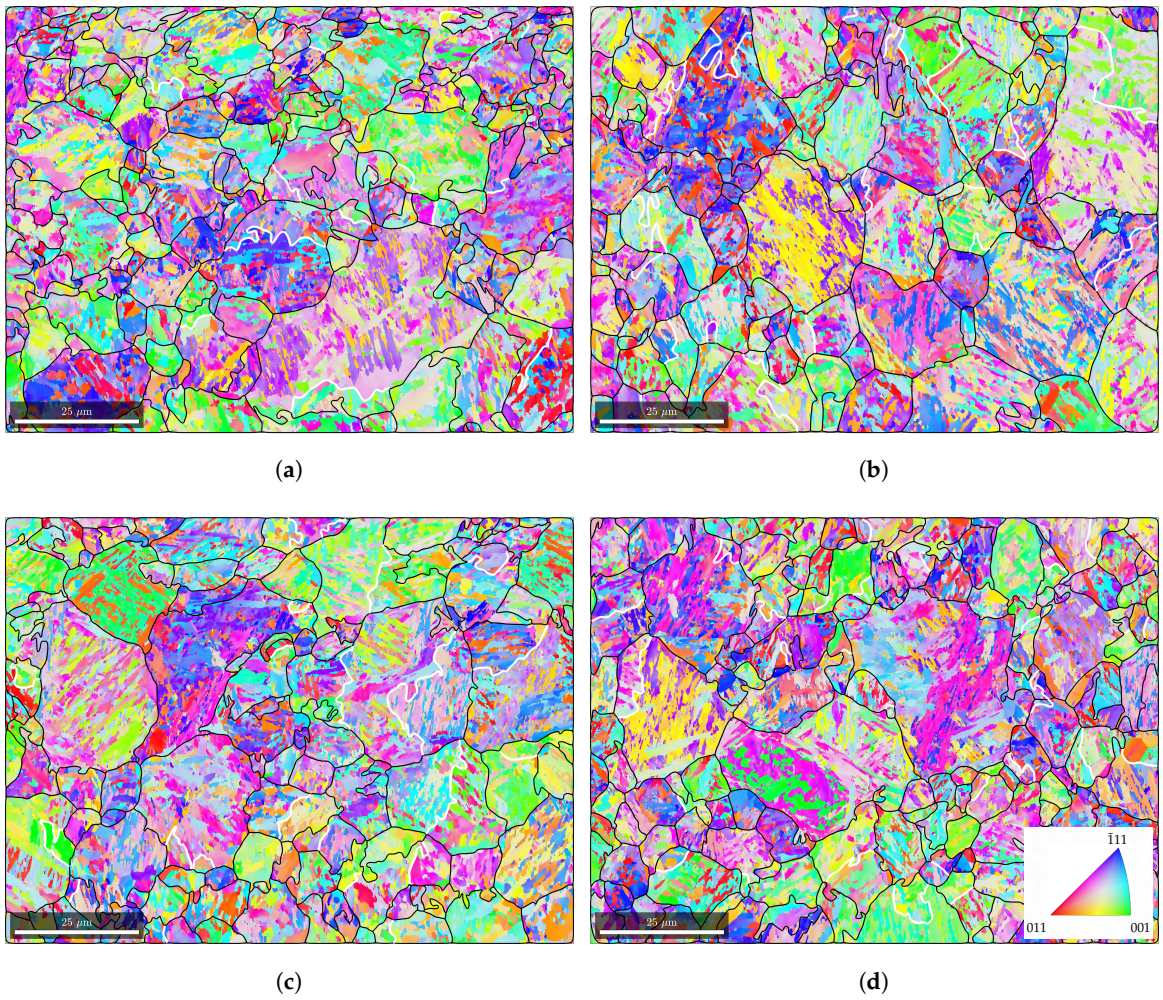

(**a**) (**b**)

(**c**) (**d**)

Figure 5. EBSD map in an inverse pole figure color scheme with superimposed prior austenite grain boundaries (black) and recrystallization twin boundaries (white): (**a**) A1, (**b**) A2, (**c**) A3, (**d**) A4.

Moreover, the CPP packets (in the following, these are referred to as packets) are calculated, which are shown in Appendix A. For the grain reconstruction, the threshold misorientation angle indicating a grain boundary is defined with $\theta_{\text{crit}} = 5°$. Since the laths cannot be clearly identified in this purely orientation-based reconstruction, the reconstructed "martensite grain" is called a "block". As a reminder, in the martensite hierarchy, blocks are the superordinate structure of the laths and a block consists of several laths of the same or a very similar orientation. The cross-section areas of the structure recorded with the EBSD system are referred to as areas A^{2D}.

According to the heat treatment, no significant differences in the grain sizes of the PAGs are expected. In Figure 6, this is checked by means of the median and mean equivalent grain diameter

$$\bar{d} = 2\sqrt{\frac{\overline{A^{2D}}}{\pi}}. \tag{2}$$

Reconstructed austenite grains which are intersected by the measurement boundary are excluded from the evaluation. Furthermore, here and in the following, grains and martensite blocks with a size smaller than 0.32 µm^2 are not evaluated. The resulting number of evaluable grains is indicated above the corresponding bars. Experiments with a higher amount of evaluable grains tend to have a smaller mean; however, a systematic influence from the heat treatment cannot be identified. Differences are therefore due to the size of the measurement section.

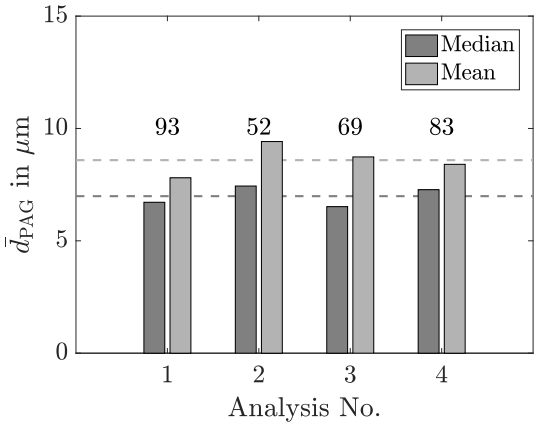

Figure 6. Comparison of mean and median prior austenite grain cross-section areas in the measured EBSD domain; numbers above bars indicate the number of evaluable grains in the domain.

In Figure 7 the empirical cumulative distribution function (ECDF) of the packet and martensite block areas—respectively, $A^{\mathrm{2D}}_{\mathrm{CPP}}$ and $A^{\mathrm{2D}}_{\mathrm{B}}$—are shown. Note the different scale of the abscissa in Figure 7b. No systematic correlation between the quenching rate and the packet areas as well as the martensite block areas can be derived.

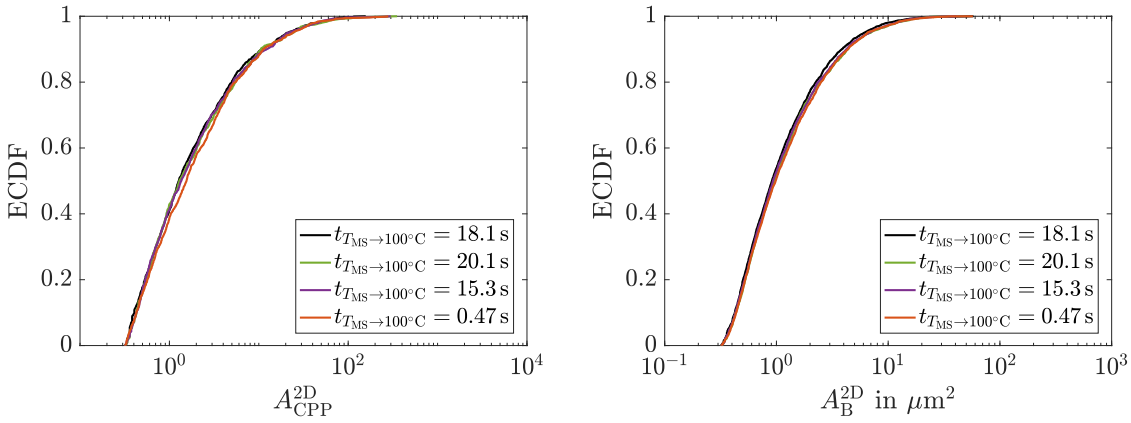

(**a**) (**b**)

Figure 7. Empirical cumulative distribution function: (**a**) normalized packet cross section areas, (**b**) normalized block cross section areas.

The diagrams in Figure 7 only represent a one-dimensional representation of the data, which is why the analyses are supplemented by a two-dimensional representation. Thus, Figure 8 shows the packet areas $A^{\mathrm{2D}}_{\mathrm{CPP}}$ over the PAG areas $A^{\mathrm{2D}}_{\mathrm{PAG}}$. In Figure 8a, the complete data of the highest and lowest tested quenching rates are documented as an example. The black dashed line depicts the highest possible packet area $A^{\mathrm{2D}}_{\mathrm{CPP}}(A^{\mathrm{2D}}_{\mathrm{PAG}})^{-1} = 1$ in this diagram. A wide spread of packet areas is identified.

In order to evaluate whether the cooling rate has an influence on the distribution of packet sizes, an attempt is made to represent the holistic trend of the data. Based on the data recorded, as shown in Figure 8a, for each quenching rate, a curve of type

$$g(x) = c_1\, x^{c_2} + c_3 \tag{3}$$

with the fitting constants c_1, c_2 and c_3 is fitted with the nonlinear least squares method to represent the data. The resulting curves are shown in Figure 8b. Based on this, the packet size depends considerably on the PAG areas. Accordingly, a larger austenite grain tends to contain larger packets. However, a clear correlation of the quenching rate with the packet areas as a function of PAG areas is not identified.

The same evaluation procedure is applied to the martensite block areas; see Figure 9. The curves fitted in Figure 9b show a lower dependency of the martensite block areas on theirs PAG area. However, again, no systematic influence of the cooling rate can be identified. The evaluation of the numbers of packets and blocks in each PAG leads to the same results; see Appendix B.

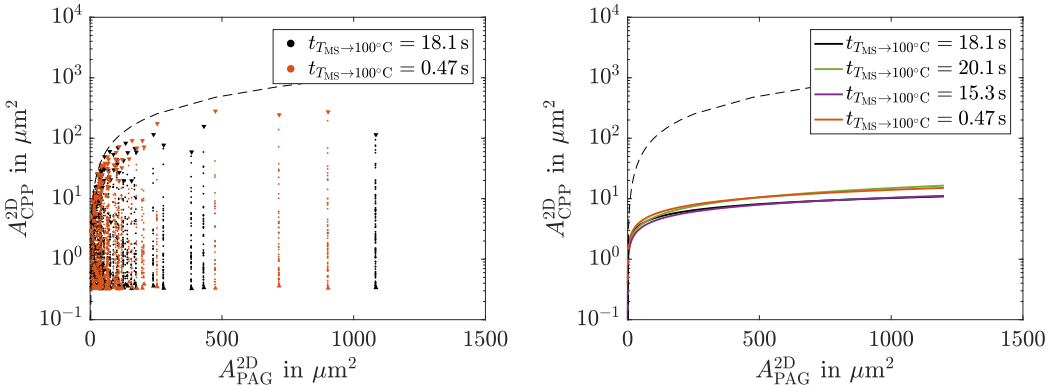

(**a**) (**b**)

Figure 8. Packet cross-section area depending on the prior austenite grain (PAG) cross-section area: (**a**) measured data, (**b**) representation of measured data with fitted curves.

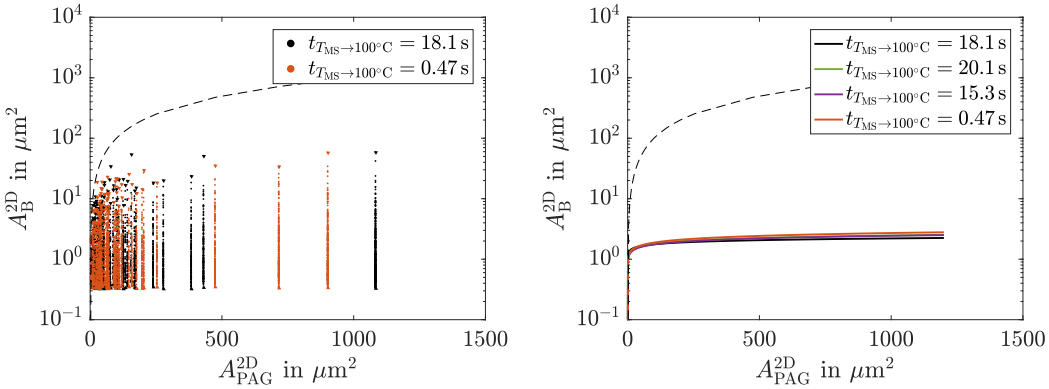

(**a**) (**b**)

Figure 9. Martensite block cross-section area depending on the prior austenite grain (PAG) cross-section area: (**a**) measured data, (**b**) representation of measured data with fitted curves.

4. Discussion

In the present investigation, specimens were heat-treated with comparable austenitization conditions but different quenching rates. A typical partitioning was omitted in order to isolate the quenching process, which is responsible for the formation of martensite. Hardness measurements were used to prove that a homogeneous microstructure was present. Accordingly, the specimens were chosen to be small enough to be able to neglect the influences of the temperature gradient in the specimen. In accordance with the current state of knowledge, a higher hardness was achieved with a more intensive quenching; see Figure 4.

Since microstructure size effects can contribute to an increase in hardness, we investigated how the quenching intensity affects the microstructure scales. For the same material, an influence of the cooling rate on the resulting block size was determined in [22]. However, with a comprehensive evaluation of the sizes of the hierarchical microstructure, no significant systematic influence of the cooling rate could be identified. The difference could be due to the size of the measurement domain, which was chosen to be larger in the present investigation. Furthermore, in [22], the authors do not describe how the values which were considered representative for the block sizes were evaluated in detail.

Due to the comparable austenitization conditions, the PAGs were expected to have the same appearance in size and shape. In order to verify this, the mean and median values of the areas were analyzed. It was shown that the median values were very similar and the mean values differed. This was due to the size of the measurement domain. However, in this study, our focus was on martensite; a possible influence of the austenite grain size was considered by the presentation of the data in relation to the austenite grain cross-section areas; see Figures 8 and 9. The following can be derived from these analyses.

The packet size as well as the number of packets is dependent on the austenite grain size. This is in agreement with the concept of pre-existing nuclei of martensite, representing crystal lattice defects in the parent austenite phase [47]. Assuming that packets are generated from these kind of nucleation points, the probability of lattice defects increases with the size of the PAG. Considering fitting curves in order to evaluate the holistic trend of block sizes with regard to PAG sizes reveals a slight dependency, which decreases with increasing $A_{\mathrm{PAG}}^{\mathrm{2D}}$. This is consistent with the Hall–Petch concept of grain boundary strengthening, where a term of type $k\,d^{-0.5}$ is added to the initial yield strength. In this term, k represents a material specific constant and d is the diameter of the grain. Thus, the results in [48] can be confirmed, where the effect of the austenite grain size on the martensitic transformation in stainless steels is investigated by simulation.

The observations of the size effect in this work are in contrast to the phenomenon observed in the majority of the literature, in which martensite sizes become smaller with increasing cooling rates [19–24]. This motivates a detailed discussion of the differences. For this purpose, relative differences of the equilibrium temperature and martensite start temperature $(T_0 - T_{\mathrm{MS}})/T_0$ as well as the chemical driving forces $\Delta G_{\mathrm{chem}}^{\mathrm{MS}}$ necessary to initiate the martensite transformation are calculated with Thermo-Calc TCFE 8 and compared. These values give an indication of the size of the energy barrier, which must be overcome. The energy barrier is composed of an additional mechanical energy component due to the displacement of the atomic structure and an interface energy component.

For comparison, references were considered in which the influence of the quenching rate was systematically investigated, T_{MS} was specified and a size effect was verifiable via corresponding images. Investigations whose temperature profiles simulated induction hardening processes and thus did not have a corresponding holding time at austenitization temperature were not considered. The limited number of references with the corresponding values are documented in Table 3.

Table 3. Comparison of relative differences between the equilibrium temperature and martensite start temperature $\frac{T_0 - T_{\mathrm{MS}}}{T_0}$, differences of Gibbs free energies at the martensite start temperature $\Delta G_{\mathrm{chem}}^{\mathrm{MS}}$ and size effects of several materials.

Material (Name)	T_{MS} in °C	Obvious Size Effect	Reference	$\frac{T_0 - T_{\mathrm{MS}}}{T_0}$ (Thermo-Calc TCFE 8)	$\Delta G_{\mathrm{chem}}^{\mathrm{MS}}$ in Jmol^{-1} (Thermo-Calc TCFE 8)
Fe-22 wt.% Ni	240	Yes	[23]	0.22	−416 *
Fe-24 wt.% Ni	187	Yes	[21]	0.29	−461 *
Fe-18 wt.% Ni	297	Yes	[21]	0.25	−615 *
18% Ni maraging steel	217	Yes	[21]	0.44	−1120
WHT1500HF	382	Yes	[27]	0.45	−1718
50CrMo4	280	No		0.52	−1875
AISI 630	140	No	[25]	0.76	−2400

* a conservative value of 0.005 wt.% C is assumed.

In [23] (Fe-22 wt.% Ni), a subsequent block formation (simultaneous in all packets and PAGs) is stated. The size dependency is explained by a thermally activated relaxation of austenite in the direct vicinity of the new blocks. A faster cooling rate leads to less relaxation, which is accompanied with a higher amount of elastic energy being introduced by the transformation. A reduced size of the block at a single block formation event is the consequence of this. The subsequent block formation mechanism is consistent with the small energy barrier indicated by the relatively low values of $(T_0 - T_{\mathrm{MS}})/T_0$

in Table 3. With a small energy barrier, the induced stresses must be relatively small. Furthermore, the chemical driving force $\Delta G_{\text{chem}}^{\text{MS}}$ is relatively small. If the energy barrier is exceeded, only a small amount of material has to be converted due to the low chemical driving force. The simultaneously induced stresses are too low to cause a mechanically driven nucleation of another block.

Another martensite formation mechanism is stated in [25]. An energy barrier crossing event is accompanied by the formation of martensite clusters consisting of several blocks and packets. These martensite clusters extend over several PAGs, which are significantly smaller than in [23]. The plausibility of this fundamentally different formation mechanism can be explained by comparing $(T_0 - T_{\text{MS}})/T_0$ and $\Delta G_{\text{chem}}^{\text{MS}}$ values with those of the material in [23]. The significantly larger ratio of $(T_0 - T_{\text{MS}})/T_0$ indicates a higher energy barrier. A significantly higher chemical driving force is therefore necessary to overcome this barrier. Higher induced stresses lead to a mechanically driven auto-nucleation mechanism (self-accommodated by the formation of corresponding martensite variants) which is stopped when the total of the additional mechanical energy and interfacial energy equals the driving force for martensite formation [25]. Higher mechanical stresses during the transformation are caused by elements such as C and Al, which influence the ratio of lattice constants [49,50]. Furthermore, smaller austenite grain sizes contribute to higher mechanical stresses due to grain boundary strengthening.

Based on the limited data available, the materials in [23,25] seem to be extreme cases. With regard to the influence of the cooling rate, the first discussed block formation mechanism could be declared as being "thermal relaxation-driven", which has a significant dependency on the cooling rate. The second mechanism could be declared as being "auto-nucleation-driven", which is invariant of the applied cooling rate. Indicators of which mechanism is present seem to be $(T_0 - T_{\text{MS}})/T_0$ and $\Delta G_{\text{chem}}^{\text{MS}}$; see Table 3. It is assumed that there is a smooth—currently unclear—transition of one mechanism into the other. Based on the results in Section 3.3, and with regard to the influence of the cooling rate, the investigated 50CrMo4 is sorted into the group of the "auto-nucleation driven" martensite formation mechanism.

The lack of size effects raises the question of the origin of the increase in hardness. This can be explained by decreased carbon segregation to lattice defects with an increasing quenching rate, which results in a higher lattice distortion and therefore higher hardness. In addition, a reduced retained austenite ratio lead to higher hardness. With the chosen methods of analysis, both effects cannot be proven beyond doubt, but an experimental confirmation is given in [22]. Furthermore, it should be noted that in [7], a morphological transition from lath to $(225)_\gamma$ martensite by increasing the cooling rate was observed. This morphological change could also increase the hardness without having an influence on T_{MS}.

5. Conclusions

The cooling rate influences the hardness of the as-quenched martensite. A detailed analysis of block and packets sizes reveals no significant dependence on the rate of cooling. It is therefore concluded that the hardness increase is an effect of reduced carbon segregation and reduced retained austenite.

No significant dependency of the martensite start temperature on the cooling rate is observed. This is consistent with an athermal initial nucleation mechanism. The number of initial nucleation points seems to depend largely on the size of the prior austenite grain: the larger the grain, the greater the probability of defects that can serve as martensite nucleation points. The block size—and thus also the packet size—is influenced by the grain size of the prior austenite grain due to grain boundary strengthening.

The invariance of the resulting martensite sizes is a consequence of the auto-nucleation-driven formation of self-accommodating martensite blocks in order to reduce the transformation-induced stresses. The values of the relative difference between the equilibrium temperature and the chemical driving force at the martensite start temperature are proposed as indicators to estimate whether the block and packets sizes are related to the cooling rate.

Author Contributions: Conceptualization, H.A., M.K., M.G. and R.M.; methodology, M.G. and M.K.; software, M.G.; formal analysis, M.G.; investigation, M.G.; writing—original draft preparation, M.G.; writing—review and editing, M.K., H.A. and R.M.; visualization, M.G.; supervision, M.K. and R.M.; project administration, H.A. All authors have read and agreed to the published version of the manuscript.

Funding: Ralf Müller would like to thank the DFG (Deutsche Forschungsgemeinschaft–German Research Foundation) for financial support–Projektnummer 172116086-SFB 926.

Acknowledgments: Marius Graf is very grateful to Cyril Cayron for providing the new version of ARPGE. Furthermore, the authors are grateful to the anonymous reviewers for carefully reading the submitted manuscript and for the numerous improvements which they suggested.

Conflicts of Interest: The authors declare no conflict of interest.

Abbreviations

The following abbreviations are used in this manuscript:

CPP	Close packet plane
EBSD	Electron backscatter diffraction
ECDF	Empirical cumulative distribution function
PAG	Prior austenite grain

Appendix A. Reconstructed Martensite Close Packet Plane Packets

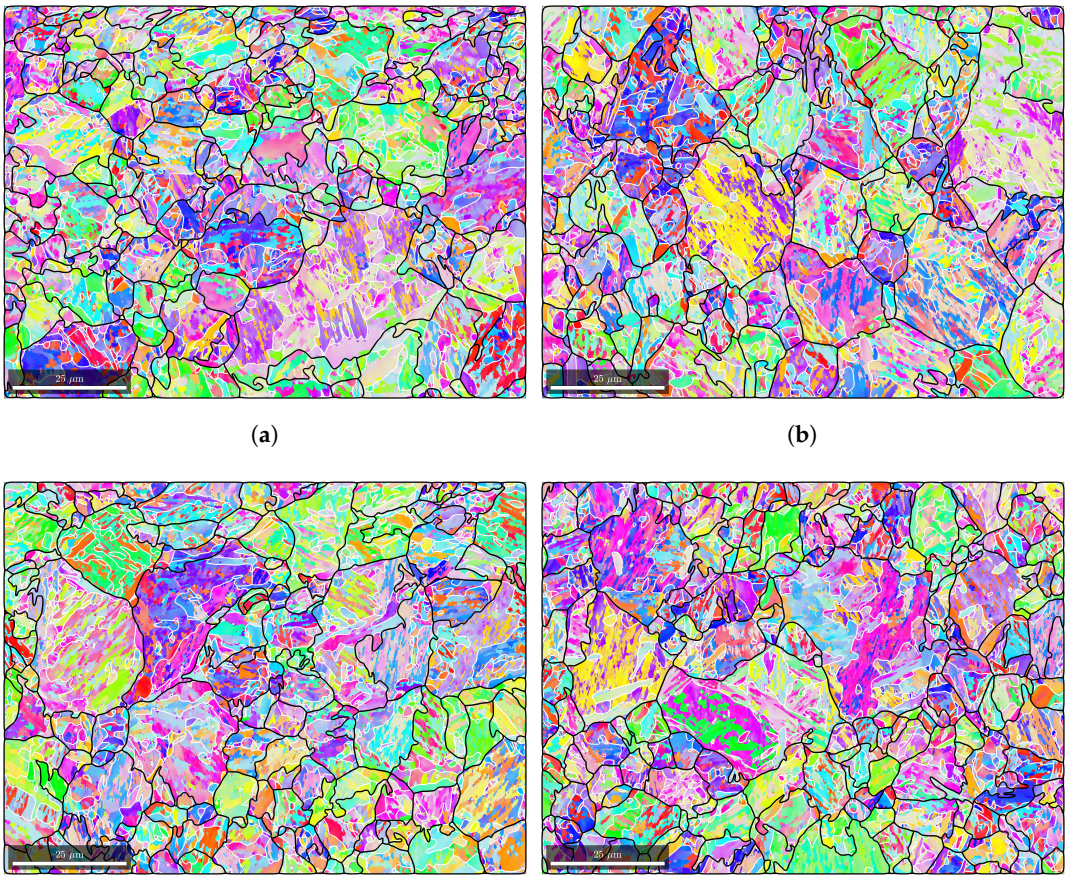

(**a**) (**b**)

(**c**) (**d**)

Figure A1. EBSD map in an inverse pole figure color scheme with superimposed prior austenite grain boundaries, recrystallization twin boundaries (black) and close packet plane packets (white). (**a**) A1, (**b**) A2, (**c**) A3, (**d**) A4.

Appendix B. Number of Close Packet Plane Packets and Blocks in Prior Austenite Grains

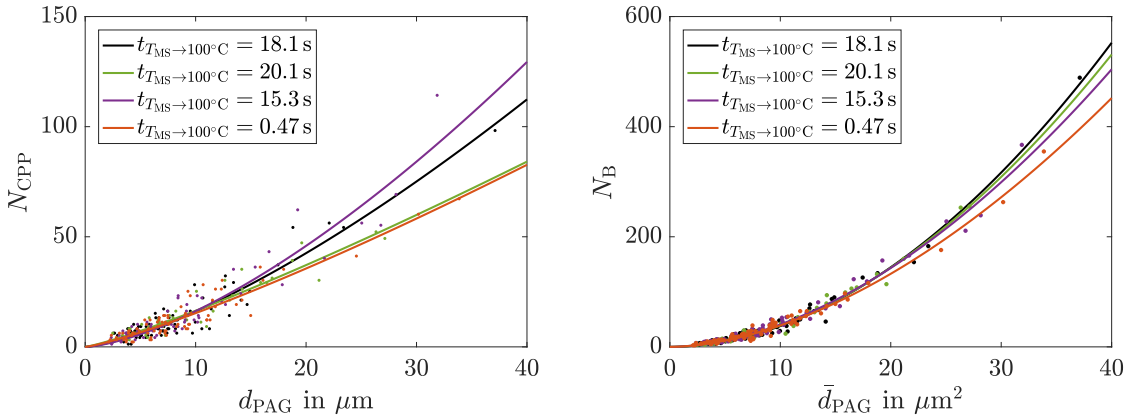

(**a**) (**b**)

Figure A2. Number of blocks in (**a**), and packets in (**b**) depending on the prior austenite grain (PAG) cross-section area.

References

1. Schäfer, B.J.; Song, X.; Sonnweber-Ribic, P.; Hartmaier, A.; ul Hassan, H. Micromechanical modelling of the cyclic deformation behavior of martensitic SAE 4150–A comparison of different kinematic hardening models. *Metals* **2019**, *9*, 368. [CrossRef]
2. Welschinger, F.; Köbler, J.; Andrä, H.; Müller, R.; Schneider, M.; Staub, S. Efficient Multiscale Methods for Viscoelasticity and Fatigue of Short Fiber-Reinforced Polymers. In *Key Engineering Materials*; Trans Tech Publ.: Baech, Switzerland, 2019; Volume 809, pp. 473–479.
3. Maki, T. Microstructure and mechanical behaviour of ferrous martensite. In *Materials Science Forum*; Trans Tech Publ.: Baech, Switzerland, 1990; Volume 56, pp. 157–168.
4. Davies, R.G.; Magee, C.L. Influence of austenite and martensite strength on martensite morphology. *Metall. Trans.* **1971**, *2*, 1939–1947.
5. Krauss, G.; Marder, A.R. The morphology of martensite in iron alloys. *Metall. Trans.* **1971**, *2*, 2343. [CrossRef]
6. Maki, T.; Shimooka, S.; Umemoto, M.; Tamura, I. The morphology of strain-induced martensite and thermally transformed martensite in Fe-Ni-C alloys. *Trans. Jpn. Inst. Met.* **1972**, *13*, 400–407. [CrossRef]
7. Mirzaev, D.A.; Shtejnberg, M.M.; Ponomareaa, T.N.; Schastlivtsev, V.M. Effect of cooling rate on martensite point position. Carbon steels. *Fiz. Met. Metalloved.* **1979**, *47*, 125–135.
8. Ivanov, Y.F.; Kozlov, E.V. Bulk and surface quenching of structural steel: Morphological analysis of the structure. *Russ. Phys. J.* **2002**, *45*, 209–231. [CrossRef]
9. Maki, T. Morphology and substructure of martensite in steels. In *Phase Transformations in Steels*; Elsevier: Amsterdam, The Netherlands, 2012; pp. 34–58.
10. Morito, S.; Huang, X.; Furuhara, T.; Maki, T.; Hansen, N. The morphology and crystallography of lath martensite in alloy steels. *Acta Mater.* **2006**, *54*, 5323–5331. [CrossRef]
11. Morito, S.; Tanaka, H.; Konishi, R.; Furuhara, T.; Maki, T. The morphology and crystallography of lath martensite in Fe-C alloys. *Acta Mater.* **2003**, *51*, 1789–1799. [CrossRef]
12. Krauss, G. *Steels: Heat Treatment and Processing Principles*; ASM International: Cleveland, OH, USA, 1990; p. 497.
13. Morito, S.; Yoshida, H.; Maki, T.; Huang, X. Effect of block size on the strength of lath martensite in low carbon steels. *Mater. Sci. Eng. A* **2006**, *438*, 237–240. [CrossRef]
14. Swarr, T.; Krauss, G. The effect of structure on the deformation of as-quenched and tempered martensite in an Fe-0.2 pct C alloy. *Metall. Trans. A* **1976**, *7*, 41–48. [CrossRef]
15. Hall, E.O. The deformation and ageing of mild steel: III discussion of results. *Proc. Phys. Soc. Sect. B* **1951**, *64*, 747. [CrossRef]
16. Petch, N.J. The cleavage strength of polycrystals. *J. Iron Steel Inst.* **1953**, *174*, 25–28.

17. Furuhara, T.; Kikumoto, K.; Saito, H.; Sekine, T.; Ogawa, T.; Morito, S.; Maki, T. Phase transformation from fine-grained austenite. *ISIJ Int.* **2008**, *48*, 1038–1045. [CrossRef]
18. Morito, S.; Saito, H.; Ogawa, T.; Furuhara, T.; Maki, T. Effect of austenite grain size on the morphology and crystallography of lath martensite in low carbon steels. *ISIJ Int.* **2005**, *45*, 91–94. [CrossRef]
19. Morito, S.; Igarashi, R.; Kamiya, K.; Ohba, T.; Maki, T. Effect of cooling rate on morphology and crystallography of lath martensite in Fe-Ni alloys. In *Materials Science Forum*; Trans Tech Publ.: Baech, Switzerland, 2010; Volume 638, pp. 1459–1463.
20. Bardelcik, A.; Salisbury, C.P.; Winkler, S.; Wells, M.A.; Worswick, M.J. Effect of cooling rate on the high strain rate properties of boron steel. *Int. J. Impact Eng.* **2010**, *37*, 694–702. [CrossRef]
21. Tsuzaki, K.; Maki, T. Effect of cooling rate on the morphology of lath martensite in Fe-Ni alloys. *J. Jpn. Inst. Met.* **1981**, *45*, 126–134. [CrossRef]
22. Eggbauer, A.; Ressel, G.; Gruber, M.; Prevedel, P.; Marsoner, S.; Stark, A.; Ebner, R. Different cooling rates and their effect on morphology and transformation kinetics of martensite. In Proceedings of the International Conference on Martensitic Transformations, Chicago, IL, USA, 11 April 2018; Springer: Berlin, Germany, 2018; pp. 35–40.
23. Loewy, S.; Rheingans, B.; Meka, S.R.; Mittemeijer, E.J. Modulated martensite formation behavior in Fe–Ni-based alloys; athermal and thermally activated mechanisms. *J. Mater. Res.* **2015**, *30*, 2101–2107. [CrossRef]
24. Shtejnberg, M.M.; Mirzaev, D.A.; Ponomareva, T.N. Gamma → alpha transformation during cooling of Fe-Mn alloys. *Fiz. Met. Metalloved.* **1977**, *43*, 166–172.
25. Villa, M.; Pantleon, K.; Reich, M.; Kessler, O.; Somers, M.A.J. Kinetics of anomalous multi-step formation of lath martensite in steel. *Acta Mater.* **2014**, *80*, 468–477. [CrossRef]
26. Liu, H.; Li, H.; Li, Z.; He, L. Effects of heating and quenching processing parameters on phase transformation of 55CrMo steel. *J. Mater. Eng. Perform.* **2018**, *27*, 5254–5270. [CrossRef]
27. Hu, K.; Zhou, G.; Liu, J. Effects of Austenitizing and Quenching Parameters on Microstructures and Mechanical Properties of Press Hardened WHT1500HF Steel. *Mater. Perform. Charact.* **2018**, *7*, 316–326. [CrossRef]
28. Javaheri, V.; Kolli, S.; Grande, B.; Porter, D. Insight into the induction hardening behavior of a new 0.40% C microalloyed steel: Effects of initial microstructure and thermal cycles. *Mater. Charact.* **2019**, *149*, 165–183. [CrossRef]
29. Eggbauer, A.; Lukas, M.; Ressel, G.; Prevedel, P.; Mendez-Martin, F.; Keckes, J.; Stark, A.; Ebner, R. In situ analysis of the effect of high heating rates and initial microstructure on the formation and homogeneity of austenite. *J. Mater. Sci.* **2019**, *54*, 9197–9212. [CrossRef]
30. Vieweg, A.; Ressel, G.; Prevedel, P.; Marsoner, S.; Ebner, R. Effects of the inductive hardening process on the martensitic structure of a 50CrMo4 steel. *HTM J. Heat Treat. Mater.* **2017**, *72*, 3–9. [CrossRef]
31. Vieweg, A.; Ressel, G.; Prevedel, P.; Raninger, P.; Panzenböck, M.; Marsoner, S.; Ebner, R. Induction hardening: Differences to a conventional heat treatment process and optimization of its parameters. In Proceedings of the IOP Conference Series: Materials Science and Engineering, Bali, Indonesia, 19–20 March 2016; Volume 119, p. 012019.
32. Vieweg, A.; Povoden-Karadeniz, E.; Ressel, G.; Prevedel, P.; Wojcik, T.; Mendez-Martin, F.; Stark, A.; Keckes, J.; Kozeschnik, E. Phase evolution and carbon redistribution during continuous tempering of martensite studied with high resolution techniques. *Mater. Des.* **2017**, *136*, 214–222. [CrossRef]
33. Vieweg, A.E.; Ressel, G.; Raninger, P.; Prevedel, P.; Marsoner, S.; Ebner, R. Comparing fast inductive tempering and conventional tempering: Effects on microstructure and mechanical properties. *Metall. Res. Technol.* **2018**, *115*, 407. [CrossRef]
34. Vieweg, A.; Raninger, P.; Prevedel, P.; Ressel, G.; Ecker, W.; Marsoner, S.; Ebner, R. Experimentelle und numerische Untersuchung des induktiven Anlassens eines Vergütungsstahles. *HTM J. Heat Treat. Mater.* **2017**, *72*, 199–204. [CrossRef]
35. Schastlivtsev, V.M.; Mirzaev, D.A.; Yakovleva, I.L. *Structure of Heat Treated Steel*; Metallurgiya Publ.: Moscow, Russia, 1994.
36. Mirzaev, D.A.; Korzunov, S.E.; Schastlivtsev, V.M.; Yakovleva, I.L. The influence of cooling rate in hardening on the quantity of residual austenite and the hardness of carbon steels. *Fiz. Met. Metalloved.* **1983**, *56*, 1033–1035.
37. Mirzaev, D. Martensite Points in Fe–C Alloys. *Fiz. Met. Metalloved.* **1987**, *63*, 764–767.

38. Van Bohemen, S.M.C.; Sietsma, J. Kinetics of martensite formation in plain carbon steels: critical assessment of possible influence of austenite grain boundaries and autocatalysis. *Mater. Sci. Technol.* **2014**, *30*, 1024–1033. [CrossRef]
39. Loewy, S.; Rheingans, B.; Meka, S.R.; Mittemeijer, E.J. Unusual martensite-formation kinetics in steels: Observation of discontinuous transformation rates. *Acta Mater.* **2014**, *64*, 93–99. [CrossRef]
40. Schäfer, B.J.; Sonnweber-Ribic, P.; Hartmaier, A.; ul Hassan, H. Micromechanical Modelling of the Influence of Strain Ratio on Fatigue Crack Initiation in a Martensitic Steel-A Comparison of Different Fatigue Indicator Parameters. *Materials* **2019**, *12*, 2852. [CrossRef] [PubMed]
41. Schäfer, B.J.; Sonnweber-Ribic, P.; Hartmaier, A.; ul Hassan, H. Micromechanical Modeling of Fatigue Crack Nucleation around Non-Metallic Inclusions in Martensitic High-Strength Steels. *Metals* **2019**, *9*, 1258. [CrossRef]
42. Cayron, C. ARPGE: A computer program to automatically reconstruct the parent grains from electron backscatter diffraction data. *J. Appl. Crystallogr.* **2007**, *40*, 1183–1188. [CrossRef] [PubMed]
43. Bachmann, F.; Hielscher, R.; Schaeben, H. Texture analysis with MTEX – free and open source software toolbox. In *Solid State Phenomena*; Trans Tech Publ.: Baech, Switzerland, 2010; Volume 160, pp. 63–68.
44. Bergmann, R.; Chan, R.H.; Hielscher, R.; Persch, J.; Steidl, G. Restoration of manifold-valued images by half-quadratic minimization. *arXiv* **2015**, arXiv:1505.07029.
45. Kurdjumov, G.; Sachs, G. Over the mechanisms of steel hardening. *Z. Phys* **1930**, *64*, 325–343.
46. Nyyssönen, T.; Peura, P.; Kuokkala, V.T. Crystallography, morphology, and martensite transformation of prior austenite in intercritically annealed high-aluminum steel. *Metall. Mater. Trans. A* **2018**, *49*, 6426–6441. [CrossRef]
47. Olson, G.; Cohen, M. A perspective on martensitic nucleation. *Annu. Rev. Mater. Sci.* **1981**, *11*, 1–32. [CrossRef]
48. Yeddu, H.K. Phase-field modeling of austenite grain size effect on martensitic transformation in stainless steels. *Comput. Mater. Sci.* **2018**, *154*, 75–83. [CrossRef]
49. Nishiyama, Z. *Martensitic Transformation*; Elsevier: Amsterdam, The Netherlands, 2012.
50. Van Bohemen, S.M.C.; Morsdorf, L. Predicting the Ms temperature of steels with a thermodynamic based model including the effect of the prior austenite grain size. *Acta Mater.* **2017**, *125*, 401–415. [CrossRef]